Separating galaxies from the cluster dark matter halo in Abell 611

A. Monna,[1,2]★ S. Seitz,[1,2] M. J. Geller,[3] A. Zitrin,[4]† A. Mercurio,[5] S. H. Suyu,[6,7]
M. Postman,[8] D. G. Fabricant,[3] H. S. Hwang[9] and A. Koekemoer[8]

[1]*University Observatory Munich, Scheinerstrasse 1, D-81679 Munich, Germany*
[2]*Max Planck Institute for Extraterrestrial Physics, Giessenbachstrasse, D-85748 Garching, Germany*
[3]*Harvad-Smithsonian Astrophysical Observatory, 60 Garden St., Cambridge, MA 02138, USA*
[4]*Cahill Center for Astronomy and Astrophysics, California Institute of Technology, MS 249-17, Pasadena, CA 91125, USA*
[5]*INAF/Osservatorio Astronomico di Capodimonte, Via Moiariello 16, I-80131 Napoli, Italy*
[6]*Max-Planck-Institut für Astrophysik, Karl-Schwarzschild-Str 1, D-85741 Garching, Germany*
[7]*Institute of Astronomy and Astrophysics, Academia Sinica, PO Box 23-141, Taipei 10617, Taiwan*
[8]*Space Telescope Science Institute, 3700 San Martin Drive, Baltimore, MD 21208, USA*
[9]*School of Physics, Korea Institute for Advanced Study, 85 Hoegiro, Dongdaemun-gu, Seoul 02455, Korea*

ABSTRACT

We investigate the mass content of galaxies in the core of the galaxy cluster Abell 611. We perform a strong lensing analysis of the cluster core and use velocity dispersion measurements for individual cluster members as additional constraints. Despite the small number of multiply-imaged systems and cluster members with central velocity dispersions available in the core of A611, the addition of velocity dispersion measurements leads to tighter constraints on the mass associated with the galaxy component, and as a result, on the mass associated with the dark matter halo. Without the spectroscopic velocity dispersions, we would overestimate the mass of the galaxy component by a factor of ∼1.5, or, equivalently, we would underestimate the mass of the cluster dark halo by ∼5 per cent. We perform an additional lensing analysis using surface brightness (SB) reconstruction of the tangential giant arc. This approach improves the constraints on the mass parameters of the five galaxies close to the arc by a factor up to ∼10. The resulting parameters are in good agreement with the $\sigma - r_{tr}$ scaling relation derived in the pointlike analysis. The galaxy velocity dispersions resulting from the SB analysis are consistent at the 1σ confidence level with the spectroscopic measurements. In contrast, the truncation radii for 2–3 galaxies depart significantly from the galaxy scaling relation and suggest differences in the stripping history from galaxy to galaxy.

Key words: gravitational lensing: strong – galaxies: clusters: general – galaxies: haloes – dark matter.

1 INTRODUCTION

Galaxies, and to a larger extent, clusters of galaxies, are dominated by dark matter (DM). Although DM cannot be observed directly, it can be detected through its gravitational effects. Thus gravitational lensing is a powerful tool for investigating the distribution of dark matter (e.g. see Schneider 2003; Bartelmann 2010; Kneib & Natarajan 2011). Lensing allows a direct probe of the total projected mass density of the lens. In the case of strong lensing (SL) by galaxy clusters, the location and redshift of sets of multiple images enable mapping of the mass–density distribution. To disentangle the cluster-scale dark halo (DH) component from the galaxies' contribution, additional constraints sensitive to only one

of the two components are necessary (Eichner et al. 2013; Monna et al. 2015).

A common assumption is that the DM content of galaxies scales in proportion to their light (e.g. see Koopmans et al. 2006). Luminosity scaling relations allow estimates of some properties of the galaxy dark haloes including their mass or central velocity dispersion and their extent. Weak and strong lensing analyses reveal that the extent of a galaxy's DM halo also depends on its environment (e.g. see Narayan 1998; Geiger & Schneider 1999; Halkola, Seitz & Pannella 2007; Limousin et al. 2007). Galaxy–galaxy lensing analyses show that typical radii of dark matter haloes are of the order of hundreds of kpc (Limousin et al. 2007; Brimioulle et al. 2013). In denser environment, like galaxy clusters (Limousin et al. 2007, 2009), galaxies are stripped during interactions with each other and with the smooth extended cluster dark matter halo. Simulations predict that galaxies in the cluster core should be strongly truncated (Merritt 1983; Limousin et al. 2009) in agreement

with lensing results. However, uncertainties in the measurements of the truncation radii are large (Natarajan, Kneib & Smail 2002; Halkola, Seitz & Pannella 2007; Limousin et al. 2007; Donnarumma et al. 2011).

In parametric SL analysis, the mass of a galaxy is often represented by a velocity dispersion. For a singular isothermal sphere, $M_{tot} \propto \sigma^2 r_{tr}$ (Elíasdóttir et al. 2007), where σ is the central velocity dispersion and r_{tr} is the halo truncation radius. Galaxy velocity dispersions are inferred directly from their luminosity through the Faber–Jackson relation ($L_e \propto \sigma_0^\alpha$) (Faber & Jackson 1976). The respective mass is then estimated through the luminosity–velocity dispersion–mass scaling relations. However, large scatter in the Faber–Jackson relation inherently introduces modelling biases in lensing analyses.

Direct measurement of the velocity dispersions of individual cluster members allows a more direct estimate of their total mass, independent of the lensing signal. Spectroscopic velocity dispersion measurements are thus useful for separating the galaxy component from the global cluster DM halo. Monna et al. (2015) show that using velocity dispersion measurements in an SL analysis sets stronger constraints on the galaxy dark matter haloes and breaks the internal degeneracy between their mass profile parameters. By using Hectospec (Fabricant et al. 2005, 2013) velocity dispersions for $\sim$15 cluster members in the core of the galaxy cluster Abell 383, Monna et al. (2015) improve constraints on the galaxy luminosity scaling relations by 50 per cent. Furthermore, surface brightness (SB) reconstruction of the giant arc in Abell 383 measures the extent of the DM haloes of some cluster members near the arc.

Here we investigate a second cluster, Abell 611 (A611 hereafter) at $z_{cl} \sim 0.288$. Several previous SL analyses derive a mass distribution for A611 focusing on different aspects of mass modelling through SL. For example, Richard et al. (2010) analyse 20 galaxy clusters from the Local Cluster Substructure Survey (LoCuSS), including A611, to constrain the total mass in cluster cores and to compare them with X-ray measurements. Donnarumma et al. (2011) combine SL and X-ray analyses of A611 and tested different approaches for modelling the mass associated with the cluster galaxy component. Within the cluster core ($r < 100$ kpc), SL and X-ray mass measurements agree well, but in the outer region there are discrepancies. The disagreement at large radius suggests an incorrect estimate of the relative contributions of the baryonic and DM components to the cluster mass as a result of the degeneracy between the galaxy and the smooth large-scale dark matter components. Newman et al. (2009, 2013a) combine kinematic data with strong and weak lensing to model the mass distribution of the cluster from the very central region out to well beyond the virial radius. They use measurement of the Brightest Cluster Galaxy (BCG) velocity dispersion to constrain its stellar mass and thus to disentangle the baryonic and DM components in the very core. A Navarro-Frenk and White (NFW, Navarro et al. 1996) profile fails to describe the cluster DM alone; shallower profiles fit the data better. More recently, Zitrin et al. (2015) presented a statistical weak and strong lensing analysis of the complete cluster sample of the Cluster Lensing and Supernovae with Hubble survey (CLASH, see Postman et al. 2012), including A611. They examine the effect of different mass parametrizations on the resulting mass model and show that systematic differences of 40 per cent in the projected surface mass density can result from various lensing degeneracies.

We use a set of spectroscopic velocity dispersions measured with Hectospec (see Fabricant et al. 2005, 2013) mounted on the multiple mirror telescope (MMT) to improve constraints on the mass

Table 1. CLASH photometric data set: column (1) filters, column (2) *HST* instrument, column (3) 5σ magnitude depth within 0.6 arcsec aperture.

Filter	Instrument	5σ depth
F225W	WFC3/UVIS	25.4
F275W	WFC3/UVIS	25.6
F336W	WFC3/UVIS	26.0
F390W	WFC3/UVIS	26.5
F435W	ACS/WFC	26.3
F475W	ACS/WFC	26.7
F606W	ACS/WFC	27.0
F775W	ACS/WFC	26.2
F814W	ACS/WFC	26.7
F850LP	ACS/WFC	25.9
F105W	WFC3/IR	26.9
F110W	WFC3/IR	26.9
F125W	WFC3/IR	26.8
F140W	WFC3/IR	26.9
F160W	WFC3/IR	26.7

distribution of A611 and its mass components. We carry out an SL analysis for A611, both with and without the velocity dispersion measurements and examine the impact of these measurements in constraining the mass both in galaxies and in the dark matter halo. We also use the SB morphology of the giant arc to refine constraints on five cluster galaxies neighbouring the arc.

Section 2 describes the photometric and spectroscopic data sets. Section 3 describes the SL analysis, the mass components included in the mass model and the lensed systems used as constraints. The SL analysis results are shown in Section 4. We discuss the improvements resulting from the use of velocity dispersion measurements in the lensing analysis. Section 5 discusses the SB reconstruction of the giant tangential arc. We conclude in Section 6. We assume a cosmological model with Hubble constant $H_0 = 70$ km s^{-1} Mpc^{-1} and density parameters $\Omega_m = 0.3$ and $\Omega_\Lambda = 0.7$. Magnitudes are in the AB system.

2 PHOTOMETRIC AND SPECTROSCOPIC DATA SET

A611 was observed in 2012 during the *Hubble Space Telescope* (*HST*) Cycle 19, as part of the CLASH survey. It was observed with the *HST* Advanced Camera for Surveys (*HST*/ACS) and the Wide Field Camera 3 (*HST*/WFC3) UVIS and IR cameras providing deep photometry in 15 different *HST* filters, to a depth of roughly $\sim$27AB (3σ). The photometric data set[1] was processed with the `Mosaic-drizzle` pipeline (see Koekemoer et al. 2011) to generate mosaic drizzled images with a common scale of 65 mas pixel^{-1}, centred on the cluster. The field of view (FOV) is $\sim$3.5 arcmin $\times$ 3.5 arcmin in the ACS filters and $\sim$2 arcmin $\times$ 2 arcmin in the WFC3IR images. In Table 1, we list the filters of the photometric data with the respective 5σ depths. We generate multiband photometric catalogues of fluxes extracted within 0.6 arcsec (9 pixels) diameter aperture using SExtractor 2.5.0 (Bertin & Arnouts 1996) in dual image mode. We use the weighted sum of all of the WFC3IR images as the detection image.

We measured redshifts and velocity dispersions with the Hectospec fibre spectrograph mounted on the MMT (Fabricant

---

[1] The CLASH photometric dataset (see Postman et al. 2012) is public and available at http://archive.stsci.edu/prepds/clash/

Table 2. List of cluster members with measured velocity dispersion in the core of A611. Column 1 gives the ID, Columns 2 and 3 give the RA and Dec. in degrees, Column 4 the spectroscopic redshift and Column 5 the `auto_mag` extracted with SEXTRACTOR in the *F*814*W* filter. Column 6 provides the effective radius measured with GALFIT in the *HST*/*F*814*W* band, and Column 7 lists the measured central velocity dispersion.

ID	RA J2000	Dec. J2000	z_{sp}	mag_{F814W}	R_{eff} (kpc)	σ_{sp} (km s^{-1})
BCG	120.236 76	36.056 57	0.287	16.6	40.0	330 ± 19
GR	120.225 30	36.055 98	0.291	19.2	5.4	185 ± 25
G2	120.240 33	36.059 50	0.283	20.0	3.4	124 ± 45
G4	120.238 50	36.061 41	0.281	19.9	1.9	214 ± 72
243	120.229 77	36.053 94	0.287	19.9	1.3	251 ± 37
446	120.213 20	36.068 16	0.286	20.5	2.3	293 ± 105
123	120.250 97	36.042 91	0.283	19.0	9.0	251 ± 24
533	120.253 50	36.075 86	0.290	19.4	3.5	249 ± 56
489	120.256 70	36.068 33	0.284	19.4	2.9	235 ± 42
248	120.227 17	36.055 02	0.295	20.7	1.3	231 ± 81
159	120.259 52	36.047 21	0.283	19.4	2.4	228 ± 41
345	120.252 13	36.058 61	0.291	19.1	4.1	221 ± 28
316	120.223 61	36.058 19	0.297	19.6	2.2	217 ± 43
402	120.251 58	36.061 92	0.288	19.1	4.2	208 ± 19
380	120.215 55	36.063 29	0.287	20.3	2.0	178 ± 44
137	120.237 92	36.046 91	0.279	20.4	1.3	156 ± 54
512	120.213 46	36.069 96	0.278	20.3	2.2	139 ± 54

et al. 2005). Hectospec has 300 fibres deployable over a 1 degree field. The instrument has 1.5 arcsec fibres and the spectra cover the wavelength range 3500–9150 Å. The resolution is of 5.5 Å full width at half-maximum, which corresponds to 105 km s^{-1} at 6000 Å. We acquired data under variable conditions with typical seeing of 0.9 arcsec on 2010 February 9, April 5 and April 9–10, on 2011 November 22–23, and on 2013 October 8 and November 28 (Fabricant et al. 2013). The typical integration time was 1 h. All redshifts are published in Lemze et al. (2013).

Within 1.5 arcmin of the cluster centre, the Hectospec data provide redshifts for 27 cluster members and central velocity dispersions for 17 of these members. We include a central velocity dispersion here only when its uncertainty is $\lesssim 40$ per cent of the dispersion.

We extract the velocity dispersions from the Hectospec spectra by applying the UNIVERSITY OF LYON SPECTROSCOPIC ANALYSIS SOFTWARE7 (ULYSS; Koleva et al. 2009). Single age stellar population models calculated with the PEGASE-HR code (Le Borgne et al. 2004) and the MILES stellar library (Sánchez-Blázquez et al. 2006) provide the basis for fitting the observed spectrum. We limit the spectral fitting range to 4100–5500 Å rest-frame wavelengths where we obtain the smallest velocity dispersion errors and the most stable velocity dispersions (Fabricant et al. 2013). Based on the measured line spread function, we convolve models to the wavelength dependent spectral resolution of the Hectospec data (Fabricant et al. 2013). We convolve models that are parametrized by age and metallicity with the line-of-sight velocity dispersion; we then use χ^2 minimization to determine the best-fitting age, metallicity and velocity dispersion. Fabricant et al. (2013) discuss the details of these measurements. Zahid et al. (2016) carry out a further demonstration of the excellent agreement between these measurements and those derived for the same galaxies by the SDSS.

Following Jorgensen, Franx & Kjaergaard (1995), we correct the measured velocity dispersion σ_{obs} observed with the Hectospec 1.5 arcsec aperture fibres, to estimate the galaxy central stellar velocity dispersion σ_{sp} within the effective radius of the galaxy, R$_{eff}$, according to

$$\sigma_{sp} = \sigma_{obs} \left(\frac{R_{eff}}{8 \times d/2} \right)^{-0.04}, \tag{1}$$

where *d* is the fibre aperture. We estimate the effective radii of cluster members with GALFIT (Peng et al. 2010) by fitting the SB distribution of the galaxies in the *HST*/*F*814*W* filter with de Vaucouleurs profiles. Table 2 lists all of the galaxies with measured velocity dispersions used in the lensing analysis.

3 STRONG LENSING MODELLING

We model the mass distribution in the core of A611 using the software GLEE developed by A. Halkola and S. Suyu (Suyu & Halkola 2010; Suyu et al. 2012). We use the observed positions of the multiple images as constraints throughout the analysis; thus, we refer to these models as pointlike. Spectroscopic redshifts of the lensed sources, if available, are additional constraints. The best-fitting model is found through a simulated annealing minimization in the image plane. The most probable parameters and uncertainties for the cluster mass model are then obtained from Monte Carlo Markov Chain (MCMC) sampling.

3.1 Multiple images

To reconstruct the mass distribution in the core of A611, we use three robust systems of multiple images as constraints (Fig. 1; see Newman et al. 2013a; Zitrin et al. 2015).

System 1 is a quintuply-lensed source spectroscopically confirmed at $z_{sp} = 1.56$ (the redshift has been recently revised, see Newman et al. 2013a). A central image, embedded in the BCG light, is associated with this system and is included as a constraint, for a total of six multiple images.

System 2 is a giant tangential arc at a distance of ∼18 arcsec from the BCG, passing in between five bright galaxies (G1–G5). We use the positions of the three brightest knots of the arc as constraints in the analysis. This system has a spectroscopic redshift of $z_{sp} = 0.9$.

Finally **system 3** is a quadruply-lensed source, for which no spectroscopic redshift is available. Thus its redshift is a free parameter and is optimized around the photometric redshift $z_{phot} = 1.54$ of the brightest lensed image (3.1) using a flat prior in the range [0.5, 2.5].

The positions of all the multiple images are listed in Table 3 together with their respective redshifts.
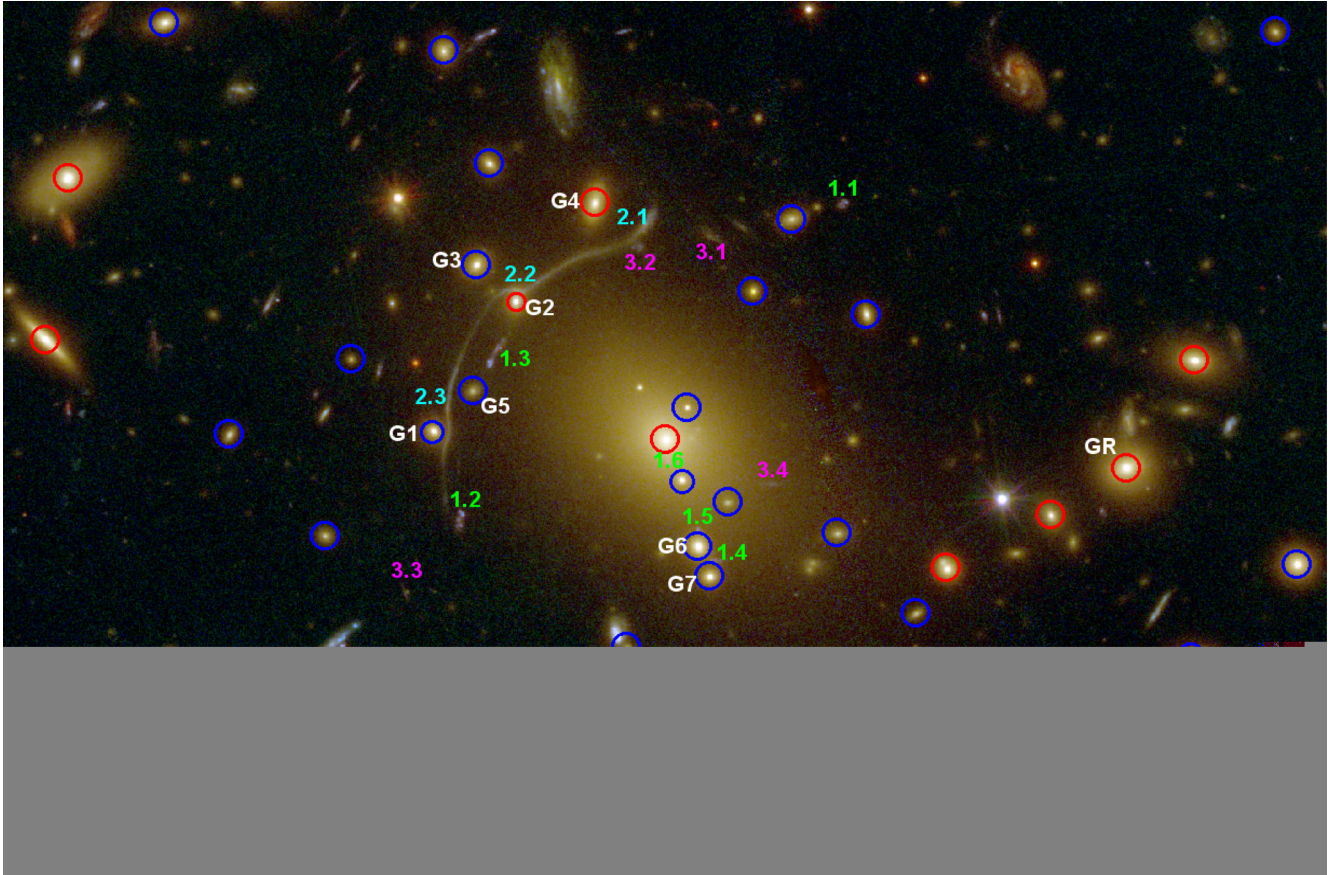
Figure 1. Colour composite image of the core (∼1.5 arcmin × 1.5 arcmin) of A611 created using the CLASH *HST* data set: blue = *F435W* + *F475W*; green = *F606W* + *F775W* + *F814W* + *F850LP*; red = *F105W* + *F110W* + *F140W* + *F160W*. Blue circles mark the cluster members included in the SL analysis. Red circles mark the galaxies with measured central velocity dispersions. 'GR' indicates the galaxy used as reference for the luminosity scaling relation. 'G1' to 'G7' are the galaxies we model individually. The three multiply-lensed systems used in the SL analysis are labelled in green (system 1), cyan (system 2) and magenta (system 3). North is up and east is left.

Table 3. Multiply-imaged systems used to constrain the SL model of A611. The columns are: Column 1 is the ID; Columns 2 and 3 RA and Dec.; Column 4 is the source redshift z_s which is spectroscopic for systems 1 and 2, and photometric for system 3 (Zitrin et al. 2015); Column 5 is the final source redshift from the SL model; Column 6 provides the difference between the observed and predicted position of each multiple image resulting from our final best cluster model (see Section 4).

ID	RA	Dec.	z_s	z_{sl}	$\delta\theta$ (arcsec)
1.1	120.232 260	36.061 430	1.56	–	1.1
1.2	120.241 820	36.055 075	1.57	–	0.6
1.3	120.241 110	36.058 144	–	–	0.4
1.4	120.235 610	36.054 100	–	–	0.1
1.5	120.235 950	36.054 732	–	–	0.2
1.6	120.236 680	36.056 140	–	–	0.8
2.1	120.237 240	36.060 997	0.91	–	1.0
2.2	120.240 480	36.059 643	–	–	0.6
2.3	120.242 150	36.057 169	0.86	–	0.6
3.1	120.235 610	36.060 708	1.54	1.68 ± 0.20	0.7
3.2	120.237 380	36.060 528	1.12	arcsec	0.3
3.3	120.243 160	36.053 450	1.52	arcsec	0.4
3.4	120.234 070	36.055 653	–	arcsec	1.1

We adopt errors of 1 arcsec on the position of the observed multiple images to account for uncertainties due to density fluctuations along the line of sight (see D'Aloisio & Natarajan 2011; Host 2012).

3.2 Cluster mass component

3.2.1 Cluster smooth large-scale halo

We describe the smooth DH mass component of the cluster with a pseudo-isothermal elliptical mass distribution (PIEMD) profile (Kassiola & Kovner 1993). Its projected surface density is

$$\Sigma(R) = \frac{\sigma^2}{2G}\left(\frac{1}{\sqrt{r_c^2 + R^2}}\right), \tag{2}$$

where σ and r_c are the halo velocity dispersion and core radius. R is the 2D radius, defined as $R^2 = x^2/(1+e)^2 + y^2/(1-e)^2$ for a profile with ellipticity $e = (1-b/a)/(1+b/a)$, where b/a is the axis ratio. The asymptotic ($b/a \to 1$, $r_c \to 0$) *Einstein* radius θ_E for this profile is

$$\theta_E = 4\pi\left(\frac{\sigma}{c}\right)^2\frac{D_{ds}}{D_s} = \Theta_E\frac{D_{ds}}{D_s} \tag{3}$$

where σ is the halo velocity dispersion, c is the speed of light, and D_s and D_{ds} are the distances to the lensed source and between

Table 5. 2D projected mass for the DH and galaxy mass components of A611. We extract the mass enclosed within the *Einstein* parameter ($\Theta_E \sim 20$ arcsec) and within a larger radius of 50 arcsec, covering the cluster core. Masses are in 10^{13} M$_\odot$.

	wo/σ	w/σ
DH		
$M_{DH}(< 20\,\text{arcsec})$	2.7 ± 0.1	2.9 ± 0.1
$M_{DH}(< 50\,\text{arcsec})$	6.6 ± 0.7	7.0 ± 0.6
Galaxies		
$M_{gal}(< 20\,\text{arcsec})$	0.5 ± 0.2	0.3 ± 0.1
$M_{gal}(< 50\,\text{arcsec})$	1.8 ± 0.4	1.2 ± 0.5

et al. 2011; Monna et al. 2015). These results are in excellent agreement with Donnarumma et al. (2011), who perform a detailed SL and X-ray analysis of A611. They test different approaches to modelling the mass associated with the cluster galaxy component. They individually optimize the mass parameters of galaxies which have strong impact on the observed lensing features just as we do in our analysis. In case 6 of their analysis, the velocity dispersion and truncation radius of six galaxies close to the lensed systems are individually optimized in the ranges [90, 190] km s^{-1} and [2, 35] kpc, respectively for σ and r_{tr}. In contrast with our approach, their scaling relation reference galaxy GR has a fixed truncation radius of 43 kpc [in agreement with results from galaxy–galaxy lensing presented in Natarajan et al. (2009)] and has $\sigma_{tr,GR}$ optimized in the range [120, 200] km s^{-1}. They perform the lensing analysis in the source plane and obtain a total reduced $\chi^2_{src} = 0.7$. The final velocity dispersion for their reference galaxy GR is $\sigma_{GR} = 150 \pm 18$ km s^{-1}, consistent at the 1σ level with our results. We also find overall agreement for the galaxies that we individually optimized. However, in both analyses, the mass parameters have large uncertainties (see Fig. 6 in the next section).

Table 4 summarizes the parameters for all of the cluster mass components, including the individually optimized galaxies, G1–G7.

To examine the impact of incorporating the measured velocity dispersions of the 17 cluster members in the lensing analysis, we model the cluster core without using the σ_{sp} ('wo/σ'). The best model wo/σ predicts the multiple images positions with a mean accuracy of 0.8 arcsec; with the measured velocity dispersions we obtain rms$_{img} = 0.7$ arcsec. Constraints on the parameters of the mass components are similar in both models (Table 4). However, the velocity dispersions σ_{sl} predicted by lensing show some deviations from the available spectroscopic measurements σ_{sp}. Fig. 4 shows the measured σ_{sp} versus the value predicted from lensing (σ_{sl}) for the model wo/σ. For comparison we also plot the results for A383 in Monna et al. (2015). In A383, the spectroscopically measured σ_{sp} and the lensing prediction agree well. The difference between A611 and A383 probably depends on the sample of cluster members for which we have σ_{sp}. In the case of Abell 383 (Monna et al. 2015), there are eight cluster members with σ_{sp} inside the cluster critical lines, and another five slightly outside. Thus in A383 we constrain the galaxy truncation radii with an error of $\sim$50 per cent. In A611, we derive much weaker constraints on the truncation radii because the sample of cluster members with measured σ_{sp} includes fewer galaxies (only five inside the critical lines) which have a strong impact on the lensing potential. Furthermore, A611 has the fewer robust SL features identified in the core of the cluster than A383 does. Fig. 5 shows the two clusters to highlight the difference between them. The figure marks the galaxies with measured σ_{sp} over a field of 50 arcsec × 50 arcsec centred on the BCG along with the multiple images and the critical curves.

The use of velocity dispersion measurements of cluster members properly weights the galaxy contribution to the total mass of the cluster. The lensing analysis wo/σ predicts $r_{tr} = 55^{+29}_{-22}$ kpc and $\sigma_{GR,wo/\sigma} = 250 \pm 63$ km s^{-1} for GR. This velocity dispersion is overestimated by a factor of 1.4 with respect to the spectroscopic measurement $\sigma_{sp,GR} = 185 \pm 25$ km s^{-1}. The total mass

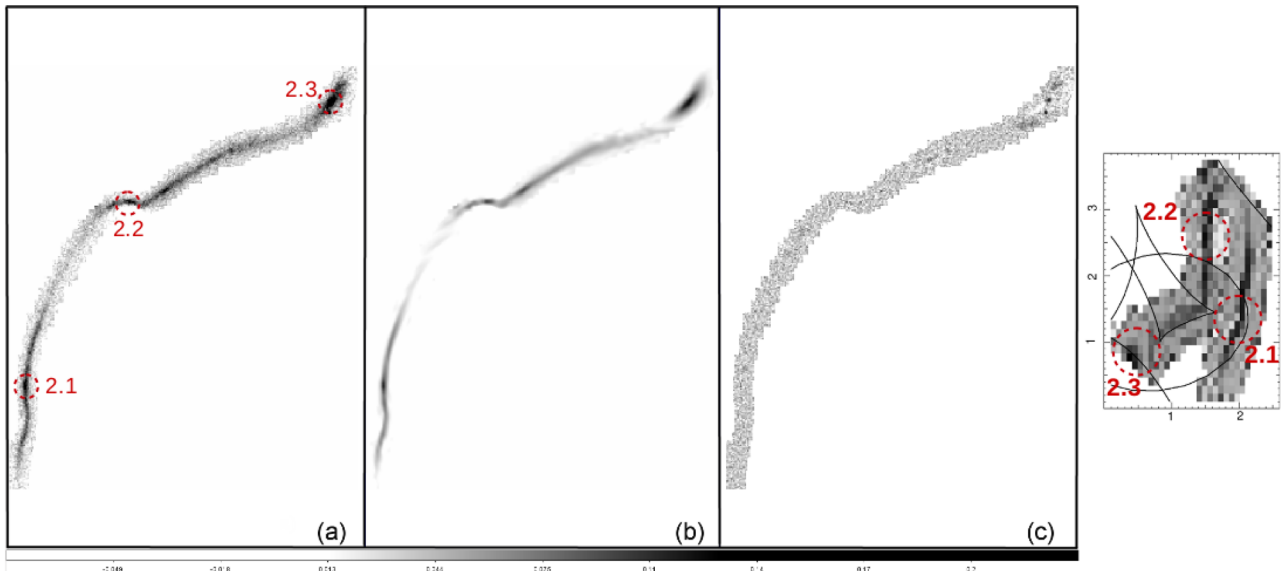**Figure 6.** SB reconstruction of the giant arc in the core of A611. Panel (a) is a cut-out ($\sim$16 arcsec × 20 arcsec) of the arc in the *HST*/ACS/*F775W* filter; panel (b) is the arc reconstruction resulting from the SB lensing modelling; panel (c) shows their residuals. On the right side we show the reconstruction of the source, which is at $z_{sp} = 0.91$. The source cut-out has size of $\sim$4 arcsec × 2.5 arcsec, the scale shown is in arcseconds. The black lines are the caustic for the source redshift. The red dotted circles mark substructures identified in the arc (panel a) and their respective position in the source plane. See text for more details.

Table 6. Final parameters of the mass components describing galaxies G1–G5 for the pointlike model and the SB model. The uncertainties are the 68 per cent confidence levels from the MCMC sampling. The radii are in kpc, the velocity dispersions are in km s^{-1}, the PAs are in degrees measured counter-clockwise from the west direction. The masses are in 10^{12} M$_\odot$.

	Pointlike model	SB model
G1		
b/a	0.8 ± 0.2	0.8 ± 0.1
PA	75 ± 11	71 ± 4
σ	$212.^{+49}_{-41}$	105 ± 3
r_{tr}	$38.^{+32}_{-27}$	2 ± 1
r_c	–	0.1 ± 0.1
M_{tot}	$1.2^{+1.6}_{-1.2}$	0.20 ± 0.05
G2		
b/a	0.7 ± 0.2	0.8 ± 0.1
PA	[86]	93 ± 6
σ	$132 \pm 39.$	107 ± 2
r_{tr}	41^{+30}_{-28}	7 ± 3
r_c	–	0.7 ± 0.2
M_{tot}	$0.5^{+0.7}_{-0.5}$	0.6 ± 0.2
G3		
b/a	0.8 ± 0.2	0.6 ± 0.1
PA	[45]	41 ± 1
σ	263^{+57}_{-53}	329 ± 4
r_{tr}	39^{+32}_{-28}	73 ± 3
r_c	–	0.1 ± 0.1
M_{tot}	$2.0^{+2.4}_{-2.0}$	5.8 ± 0.3
G4		
b/a	0.5 ± 0.2	$1^{+0.0}_{-0.01}$
PA	[82]	83 ± 3
σ	195 ± 36	279 ± 1
r_{tr}	34^{+35}_{-25}	14 ± 3
r_c	–	4 ± 1
M_{tot}	$1.0^{+1.3}_{-1.}$	0.8 ± 0.1
G5		
σ	83 ± 21	30 ± 15
r_{tr}	40^{+31}_{-27}	59^{+20}_{-30}
M_{tot}	0.2 ± 0.2	$0.5^{0.3}_{-0.4}$

associated with GR is $M_{tot,GR}^{wo/\sigma} = 2.5 \times 10^{12}$ M$_\odot$ compared with $M_{tot,GR}^{wo/\sigma} = 1.1 \times 10^{12}$ M$_\odot$ estimated using the measured σ_{sp} values in the analysis.

Overestimation of the mass of GR translates into a global over-estimate of the total galaxy mass component in the cluster. Table 5 lists the projected mass for the cluster galaxy contribution and for the large-scale DH. The mass associated with the cluster members is overestimated by a factor of ∼1.5 without use of the velocity dispersions in the analysis. Consequently, the mass associated with the large-scale DH is underestimated by ∼5 per cent in the model '*wo/σ*'. In spite of the small sample of cluster members with measured velocity dispersions in A611, these spectroscopic measurements allow proper weighting of the mass associated with the galaxies relative to the large-scale dark matter halo.

5 SURFACE BRIGHTNESS RECONSTRUCTION OF THE GIANT ARC

In the pointlike analysis, we individually optimized some of the cluster members which reside very close to multiple images and thus probably contribute significantly to the local lensing distortion. However, the mass profiles for these galaxies are actually poorly constrained by the pointlike modelling.

Here, we use the SB reconstruction of the giant arc to improve the constraints on the mass parameters of the galaxies, G1–G5, that are close to the arc by using the entire pixel to pixel lensing information encoded in the arc. The analysis is performed in the *HST*/ACS/*F775W* image. We subtract the neighbouring cluster members from the image of the arc using GALFIT (Peng et al. 2010) thus removing light that would otherwise contaminate the arc SB reconstruction. We start the SB modelling from the final best model obtained in the pointlike analysis. The SB reconstruction of giant arcs is a powerful tool for placing strong constraints on the mass distribution of the lens, but it is only effective in the local neighbourhood of the reconstructed arc. The pixel to pixel constraints associated with the giant arc are of the order of 10^3 higher than the pointlike constraints associated with the other multiple image systems used in the analysis. Thus, the minimization and the MCMC analyses are dominated by the constraints from the arc. Throughout the SB analysis we must fix the parameters of the mass components which do not play a major role in the local distortion of the giant arc. In Appendix A, we show the MCMC resulting from the pointlike analysis. The parameters describing the mass component of galaxies G1–G5 have no degeneracies with the parameters of the large-scale DH, the BCG and the reference galaxy GR. Thus through the SB reconstruction of the giant arc, the parameters describing the DH, BCG and GR are fixed to the values of the final best model of the pointlike analysis. Only the five galaxies G1–G5 close to the giant arc (see Fig. 1), are individually optimized in the SB reconstruction. Their ellipticity, PA, velocity dispersions and truncation radii are free parameters. Given the larger number of constraints provided by the SB analysis, we also release the core radii for these galaxies to infer a more detailed profile of the local mass distribution. Two of these galaxies, G2 and G4, have measured velocity dispersions (see Table 2) optimized within the spectroscopic error with a Gaussian prior. We perform the SB reconstruction through a linear inversion method (Warren & Dye 2003) which reconstructs the pixelated brightness distribution of the source, with regularization of its intensity, through a Bayesian analysis (Suyu et al. 2006).

The first model resulting from the SB reconstruction has a large reduced $\chi^2_{SB} = 1.6$. For consistency with the pointlike analysis, where we adopt larger uncertainties in the multiple images position of 1 arcsec, at this stage of the SB analysis we increase the pixel noise associated with the *HST*/ACS/*F775W* image by a factor of $\sqrt{1.6}$.

Fig. 6 shows the results of the SB reconstruction of the arc in the *F775W* filter as well as the reconstructed source. The giant arc is reconstructed well (panel b in Fig. 6) with $\chi^2_{SB} = 0.8$ on the pixel intensities and with residuals lower than 10^{-3} (panel c in Fig. 6). Large residuals remain close to the upper multiple image 2.3, where a bright compact object is clearly identified. Our reconstruction does not reproduce this object as part of the lensed system. This compact object is unlikely to be part of the lensed source. Otherwise it would be possible to identify such a substructure close to the other multiply-lensed structures of the arc as well (i.e. close to image 2.1 and 2.2). On the right side of Fig. 6, we show the source reconstruction of the lensed system. We obtain a good SB reconstruction of
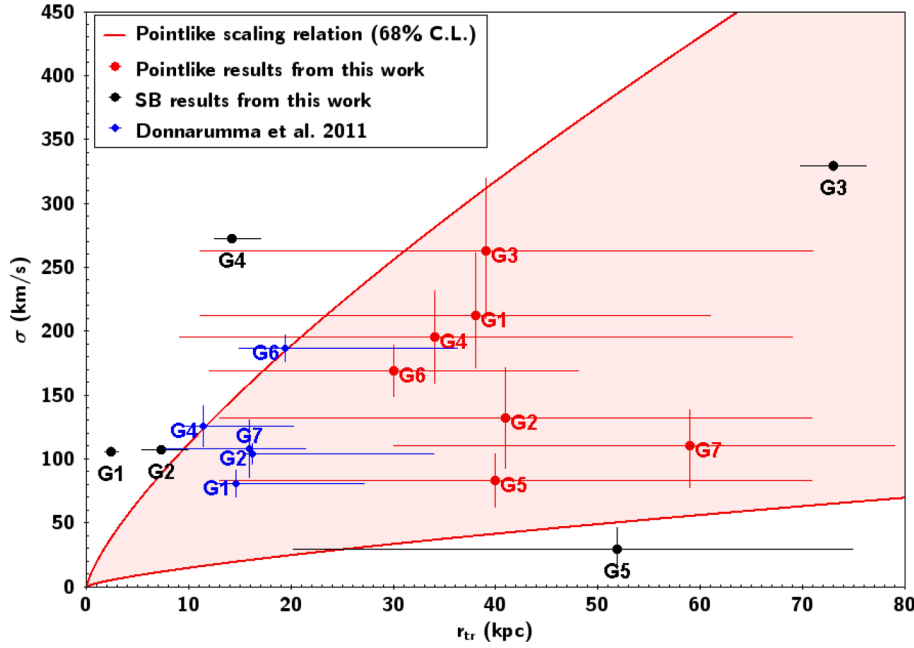
Figure 7. Velocity dispersions and truncation radii for galaxies G1–G5 resulting from the SB (black) and the pointlike (red) modelling. The red shaded region shows the cluster galaxy scaling relation derived from the pointlike analysis. In blue we plot results for the same galaxies from the pointlike SL analysis performed by Donnarumma et al. (2011). The galaxies G2, G3 and G5 are consistent at the 1σ confidence level: galaxies G1 and G4 deviate by 2σ or more.

the giant arc in the image plane. In the source plane, however, the substructures of the arc have an offset of ∼1.5–2.5 arcsec, which corresponds to ∼10 kpc at the redshift of the source.

Table 6 summarizes the resulting mass parameters for galaxies G1–G5 optimized through this analysis with their respective 1σ uncertainties. The halo axis ratio b/a and PAs are consistent with the results from the pointlike analysis, as well as with the values measured from the photometry. Only G4 obtains a considerably larger axis ratio $b/a = 1$ with respect to the $b/a = 0.5$ measured from the photometry and resulting from the pointlike model. The velocity dispersions for G2 and G4 are both consistent with the spectroscopic measurements (see Table 2), although G4 has an higher value compared with the estimates from the pointlike analysis. The other galaxies obtain velocity dispersions which depart significantly from the previous pointlike results.

Overall the SB modelling yields improved constraints on the galaxy truncation radii and masses. The truncation radii for G3, G4 and G5 agree at the 1σ level with the pointlike estimate. For G1 and G2 we obtain quite small radii (<15kpc) indicating that the dark matter haloes of these objects are highly truncated. The total mass associated with each galaxy is consistent within the 1σ uncertainties with the mass estimated through the pointlike analysis, but now the masses are better constrained by a mean factor of 70 per cent. Fig. 7 compares σ and r_{tr} derived through the SB reconstruction with the pointlike results. At the 1σ confidence level, the galaxies are consistent with the scaling relation derived in the pointlike analysis, except for G1 and G2 which deviate substantially from the relation. Fig. 7 also shows results from Donnarumma et al. (2011) for comparison. The Donnarumma et al. (2011) results for galaxies G1–G5 are generally consistent with our scaling relation and with the results from the pointlike analysis. However, they predict smaller σ and r_{tr} for these galaxies as a result of the smaller range adopted for the parameter optimization([120, 200] km s^{-1} for velocity dispersions and [2, 35] kpc for truncation radii). Nevertheless overall both approaches predict that these galaxies are highly truncated. According

to the SB reconstruction, G1 has $r_{tr,G4} = 2 \pm 1$ kpc, only twice its effective radius ($R_{eff,G1} = 1$ kpc) as measured in the *HST/F*814*W* image. This galaxy has a total mass $M_{tot,G1} = 2.0 \pm 0.5 \times 10^{11}$ M$_\odot$. Comparing its total mass with a prediction for field galaxies (e.g. Brimioulle et al. 2013), G1 has probably been stripped of 99 per cent of its original dark matter halo. G2 and G4 have also apparently lost most of their dark haloes through stripping processes (98 per cent and 97 per cent, respectively); G3 and G5 have lost 85 per cent and 90 per cent, respectively. Variations in the stripped mass may be explained by differences in the stripping processes resulting from different orbits through the cluster (Warnick, Knebe & Power 2008).

6 CONCLUSION

We use central velocity dispersion measurements for 17 members of the galaxy cluster A611 as constraints to refine an SL model for the cluster. The inclusion of velocity dispersion measurements improves determination of the mass associated with galaxies in the cluster relative to the mass contained in the extended dark matter halo. Without the spectroscopically determined σ_{sp}, the mass associated with the galaxies is overestimated by a factor ∼1.5, and consequently the mass of the large-scale dark matter is underestimated by ∼5 per cent.

In contrast with the cluster A383 (Monna et al. 2015) where the use of central velocity dispersions substantially improves constraints on the truncation radii of cluster galaxies, there is little change in these constraints in the case of A611. Errors in the truncation radii for galaxies in A611 are ∼75 per cent comparable with the errors from the SL modelling without using σ_{sp}. This result for A611 relative to A383 is due to both the size of the samples of cluster members with measured velocity and the number of lensed features. In A383 (Monna et al. 2015) there are ∼10 galaxies with measured σ_{sp} inside the critical lines and the constraints on the truncation radii improve by ∼50 per cent. In A611, there are only five galaxies inside the region probed robustly by SL. Furthermore,

A611 has only three systems of multiple images in the cluster core whereas A383 has 10.

SB reconstruction of the tangential giant arc associated with A611 does provide additional constraints on five cluster members projected near the arc. The galaxies G2 and G4 get velocity dispersions from the SB analysis which are consistent at the 1σ confidence level with the respective spectroscopic measurements. Overall the parameters of the galaxies are in agreement with the scaling relation derived in the pointlike analysis. In contrast two of these galaxies depart substantially from the galaxy scaling relation. Their small truncation radii may reflect differing stripping history among individual cluster members (Warnick et al. 2008).

More extensive samples of spectroscopically measured velocity dispersions for members of a set of clusters will eventually provide a platform for refining the relative contribution of the cluster members and the dark matter halo to the overall cluster mass distribution as a function of total cluster mass and as a function of the evolutionary state of the cluster. Combined with large redshift surveys of the central cluster region they promise insight into the stripping processes that govern the evolution of galaxies in dense cluster environments.

REFERENCES

Arnouts S., Cristiani S., Moscardini L., Matarrese S., Lucchin F., Fontana A., Giallongo E., 1999, MNRAS, 310, 540
Bartelmann M., 2010, Class. Quantum Gravity, 27, 233001
Bender R., Burstein D., Faber S. M., 1992, ApJ, 399, 462
Bertin E., Arnouts S., 1996, A&AS, 117, 393
Brimioulle F., Seitz S., Lerchster M., Bender R., Snigula J., 2013, MNRAS, 432, 1046
D'Aloisio A., Natarajan P., 2011, MNRAS, 411, 1628
Donnarumma A. et al., 2011, A&A, 528, A73
Dressler A., Lynden-Bell D., Burstein D., Davies R. L., Faber S. M., Terlevich R., Wegner G., 1987, ApJ, 313, 42
Eichner T. et al., 2013, ApJ, 774, 124
Elíasdóttir Á. et al., 2007, preprint (arXiv:0710.5636)

Faber S. M., Jackson R. E., 1976, ApJ, 204, 668
Faber S. M., Dressler A., Davies R. L., Burstein D., Lynden-Bell D., 1987, in Faber S. M., ed., Nearly Normal Galaxies. From the Planck Time to the Present. Springer-Verlag, New York, p. 175
Fabricant D. et al., 2005, PASP, 117, 1411
Fabricant D., Chilingarian I., Hwang H. S., Kurtz M. J., Geller M. J., Del'Antonio I. P., Rines K. J., 2013, PASP, 125, 1362
Focardi P., Malavasi N., 2012, ApJ, 756, 117
Geiger B., Schneider P., 1999, MNRAS, 302, 118
Halkola A., Seitz S., Pannella M., 2007, ApJ, 656, 739
Hoekstra H., Franx M., Kuijken K., Carlberg R. G., Yee H. K. C., 2003, MNRAS, 340, 609
Host O., 2012, MNRAS, 420, L18
Ilbert O. et al., 2006, A&A, 457, 841
Ilbert O. et al., 2009, ApJ, 690, 1236
Jorgensen I., Franx M., Kjaergaard P., 1995, MNRAS, 276, 1341
Jullo E., Kneib J.-P., Limousin M., Elíasdóttir Á., Marshall P. J., Verdugo T., 2007, New J. Phys., 9, 447
Kassiola A., Kovner I., 1993, in Surdej J., Fraipont-Caro D., Gosset E., Refsdal S., Remy M., eds, Proc. 31st Liege Int. Astrophys. Colloq., (LIAC 93), Gravitational Lenses in the Universe. Universite de Liege, Institut d'Astrophysique, p. 571
Kneib J.-P., Natarajan P., 2011, A&AR, 19, 47
Koekemoer A. M. et al., 2011, ApJS, 197, 36
Koleva M., Prugniel P., Bouchard A., Wu Y., 2009, A&A, 501, 1269
Koopmans L. V. E., Treu T., Bolton A. S., Burles S., Moustakas L. A., 2006, ApJ, 649, 599
Kormendy J., Bender R., 2013, ApJ, 769, L5
Le Borgne D., Rocca-Volmerange B., Prugniel P., Lançon A., Fioc M., Soubiran C., 2004, A&A, 425, 881
Lemze D. et al., 2013, ApJ, 776, 91
Limousin M., Kneib J. P., Bardeau S., Natarajan P., Czoske O., Smail I., Ebeling H., Smith G. P., 2007, A&A, 461, 881
Limousin M., Sommer-Larsen J., Natarajan P., Milvang-Jensen B., 2009, ApJ, 696, 1771
Merritt D., 1983, ApJ, 264, 24
Monna A. et al., 2015, MNRAS, 447, 1224
Narayan R., 1998, New Astron. Rev., 42, 73
Natarajan P., Kneib J.-P., Smail I., 2002, ApJ, 580, L11
Natarajan P., Kneib J.-P., Smail I., Treu T., Ellis R., Moran S., Limousin M., Czoske O., 2009, ApJ, 693, 970
Navarro J. F., Frenk C. S., White S. D. M., 1996, ApJ, 462, 563
Newman A. B., Treu T., Ellis R. S., Sand D. J., Richard J., Marshall P. J., Capak P., Miyazaki S., 2009, ApJ, 706, 1078
Newman A. B., Treu T., Ellis R. S., Sand D. J., 2013a, ApJ, 765, 25
Newman A. B., Treu T., Ellis R. S., Sand D. J., Nipoti C., Richard J., Jullo E., 2013b, ApJ, 765, 24
Peng C. Y., Ho L. C., Impey C. D., Rix H.-W., 2010, AJ, 139, 2097
Postman M. et al., 2012, ApJS, 199, 25
Richard J., Kneib J.-P., Limousin M., Edge A., Jullo E., 2010, MNRAS, 402, L44
Rusin D. et al., 2003, ApJ, 587, 143
Sánchez-Blázquez P. et al., 2006, MNRAS, 371, 703
Schneider P., 2003, preprint (astro-ph/0306465)
Suyu S. H., Halkola A., 2010, A&A, 524, A94
Suyu S. H., Marshall P. J., Hobson M. P., Blandford R. D., 2006, MNRAS, 371, 983
Suyu S. H. et al., 2012, ApJ, 750, 10
Warnick K., Knebe A., Power C., 2008, MNRAS, 385, 1859
Warren S. J., Dye S., 2003, ApJ, 590, 673
Zahid H. J., Damjanov I., Geller M. J., Hwang H. S., Fabricant D. G., 2016, ApJ, 821, 101
Zitrin A. et al., 2015, ApJ, 801, 44

APPENDIX A: MCMC SAMPLING OF THE POINTLIKE MODELS

In this section, we present the MCMC sampling of the parameters describing the mass components of A611 resulting from the point-like analysis, presented in Section 4. The colour scale corresponds to 68.3 per cent (green), 95.5 per cent (yellow) and 99.7 per cent (orange). The blue dot indicates the median of the distribution; the black cross is the best value. Fig. A1 shows the MCMC sampling for

the parameters of the smooth DH, the BCG, the reference galaxy GR and the galaxies G1 and G2. Fig. A2 shows the sampling of the mass parameters for DH, BCG, GR together with the galaxies G3, G4 and G5. In both plots, there is no degeneracy between the parameters of the galaxies in the neighbourhood of the giant arc (G1–G5) and the mass components of the large-scale halo, the BCG and the reference galaxy.
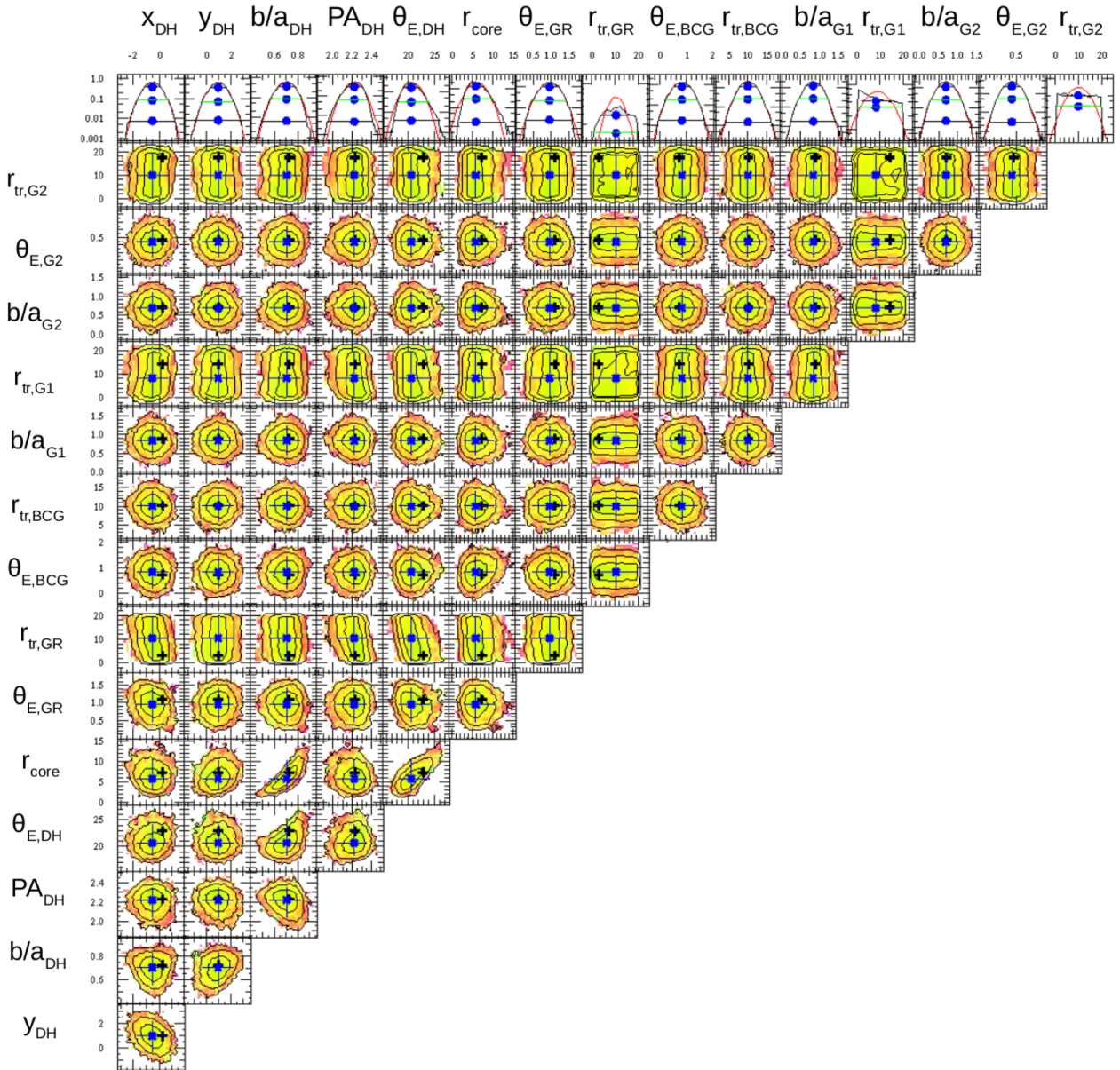
Figure A1. MCMC sampling of the parameters for the DH, BCG, GR and the galaxies G1 and G2 close to the giant arc. The coordinates x_{DH} and y_{DH} are in arcseconds with respect to the BCG position. PAs are in radians. The radii r_{core} and r_{tr} are in arcseconds. The *Einstein* radii (θ_E) are also in arcseconds for $D_{ds}/D_d = 1$.
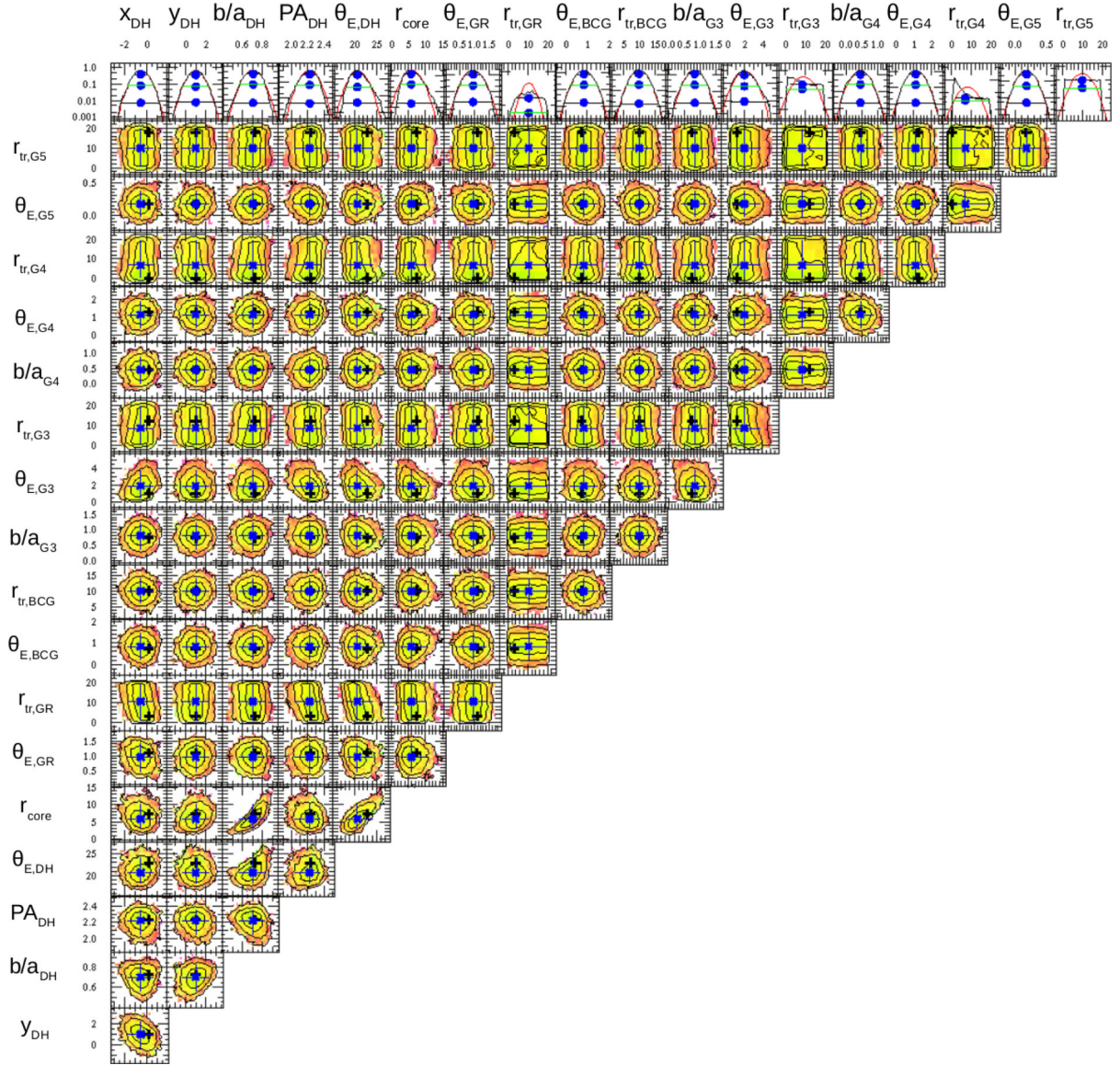
Figure A2. Results of the MCMC analysis for the parameters of the DH, GR and BCG mass components of A611, together with the mass parameters for the galaxies G3, G4 and G5. The units are as in the previous figure.

This paper has been typeset from a TeX/LaTeX file prepared by the author.